PROCEEDINGS OF SPIE

SPIEDigitalLibrary.org/conference-proceedings-of-spie

Uncertainty evaluation of a fiber-based interferometer for the measurement of absolute dimensions

Badami, Vivek, Blalock, Todd

Vivek G. Badami, Todd Blalock, "Uncertainty evaluation of a fiber-based interferometer for the measurement of absolute dimensions," Proc. SPIE 5879, Recent Developments in Traceable Dimensional Measurements III, 587903 (18 August 2005); doi: 10.1117/12.617022

SPIE.

Event: Optics and Photonics 2005, 2005, San Diego, California, United States

Downloaded From: https://www.spiedigitallibrary.org/conference-proceedings-of-spie on 10 Apr 2020 Terms of Use: https://www.spiedigitallibrary.org/terms-of-use

Uncertainty evaluation of a fiber-based interferometer for the measurement of absolute dimensions

Vivek G. Badami[*a] and Todd Blalock[b]
[a]Corning Tropel Corporation, 60 O'Connor Road, Fairport, NY 14450
[b]Lumetrics Inc., 150 Lucius Gordon Drive, West Henrietta, NY 14586

ABSTRACT

The evaluation of the measurement uncertainty of a robust all-fiber-based low-coherence interferometer for the measurement of absolute thickness of transparent artifacts is described. The performance of the instrument is evaluated by measuring the length of air-gaps in specially constructed artifacts and the observed measurement errors are discussed in the context of the uncertainty associated with them. A description of the construction of the artifacts is presented, accompanied by an uncertainty analysis to estimate the uncertainty associated with the artifacts. This analysis takes into account the dimensional uncertainty of the artifacts (including wringing effects), thermal effects, and effects of the environment on refractive index. The 'out-of-the-box' performance of the instrument is first evaluated. A maximum error of 350 nm for an air-gap of 10.1 mm is observed. A linear trend between the measured length and the error is also observed. The relative magnitude of the errors and the uncertainty associated with the error suggests that this trend is real and that a performance enhancement can be expected by mapping the error. Measurements of the artifacts are used to develop an error map of the instrument. The uncertainty associated with the predicted error is determined based on the uncertainty associated with the error. This analysis suggests that the uncertainty in the predicted error at the 2σ level may be conservatively estimated to be *(2.9L+37.5)* nm, where L is in units of mm.

Keywords: Low-coherence, interferometer, high-accuracy, uncertainty estimate, laser, absolute dimensions

1. INTRODUCTION

The ability to perform non-contact, absolute distance measurements with high precision is essential in a number of applications in science and industry. As these types of measurements move out of the laboratory and into a manufacturing environment, the need arises for the instruments to perform these measurements in a real-time mode. The most accurate methods of performing absolute distance measurements are based on optical interferometry. Some interferometric methods for absolute distance measurement are based on high-coherence laser measurements such as two-wavelength super-heterodyne detection[1] while other techniques use low-coherence interferometry. Low-coherence interferometry (LCI) is a measurement technique based on white light interferometry that led to the development of optical coherence domain reflectometry (OCDR). This one-dimensional optical ranging technique uses a low-coherence light source to obtain highly accurate distance measurements. OCDR was originally developed for locating faults in fiber optic cables and network components. The use of OCDR has since spread from fiber-optic reflectometry,[3] to Bragg grating measurements,[4] to optical coherence tomography in biological imaging applications.[5]

The demand for a robust, accurate, user-friendly, and precise instrument for use in an industrial setting led to the development of the instrument described in this paper. Early work on a robust low-coherence interferometer was done by Marcus *et al.* [6-9] of Eastman Kodak for a variety of industrial applications, including liquid layer thickness monitoring on coating hoppers, film base thickness uniformity, digital camera focus assessment, optical cell path length assessment, and CCD imager and wafer surface profile mapping. The first generation instrument was a Michelson interferometer in an autocorrelator configuration. A mechanical assembly driven by a brushless DC motor produced the path length change by moving retro-reflectors in the arms of the interferometer in a reciprocating motion. A high-accuracy determination of the sample dimensions requires a determination of the change in path length with a

[*] Contact: badamivg@corning.com; Phone (585) 388-3500; Fax: (585) 377-6332; http://www.corning.com; Corning Tropel, 60 O'Connor Road, Fairport, NY 14450, USA.

Recent Developments in Traceable Dimensional Measurements III, edited by Jennifer E. Decker, Gwo-Sheng Peng,
Proceedings of SPIE Vol. 5879 (SPIE, Bellingham, WA, 2005) · 0277-786X/05/$15 · doi: 10.1117/12.617022

Downloaded From: https://www.spiedigitallibrary.org/conference-proceedings-of-spie on 10 Apr 2020
Terms of Use: https://www.spiedigitallibrary.org/terms-of-use

commensurate degree level of accuracy. This was accomplished by using a second interferometer based on a laser source that occupied the same air path as the low-coherence interferometer. A frequency stabilized helium-neon laser was used to produce a stable fringe signal serving as a reference "clock" for the data acquisition. This "clock" produced trigger signals at constant intervals along the path length change.[10]

The next generation interferometer replaced the motor-driven bulk optics and the helium-neon laser with piezoelectric (PZT) fiber stretchers and a 1550 nm distributed-feedback (DFB) semiconductor diode laser respectively.[11] In this embodiment, the interferometer has no moving parts and utilizes telecom-grade components with long lifetimes and high reliability. The latest instrument, evaluated in this paper, incorporates additional features such as real-time data acquisition and computation to allow for rapid measurements of optical thickness in an industrial environment.

2. DESCRIPTION OF INSTRUMENT

This section briefly outlines the theory behind low-coherence interferometry and describes the principle of operation of the instrument and the instrument layout.

2.1. Theory of operation

The differences between low-coherence and high-coherence interferometry are illustrated in Fig. 1. The interference signal from a typical Michelson interferometer is represented by

$$I_d(\tau) = \frac{1}{2}\left(I_{\text{Arm1}} + I_{\text{Arm2}}\right) + \text{Re}\left\{\langle E^*_{\text{Arm1}}(t+\tau)\, E_{\text{Arm2}}(t)\rangle\right\} \tag{1}$$

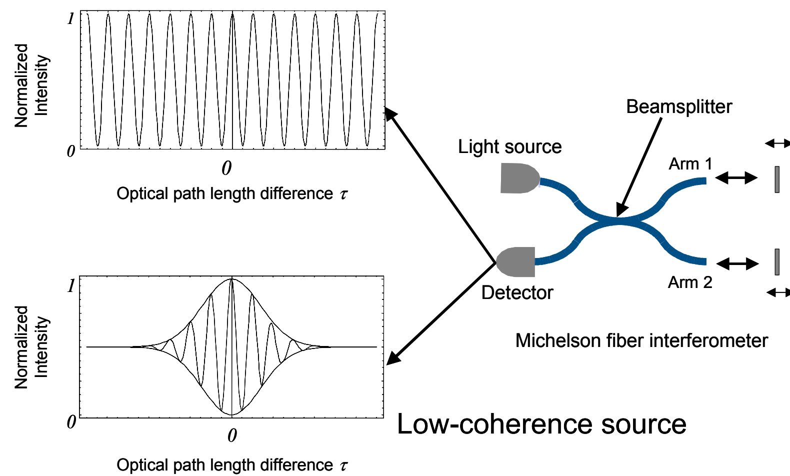

Figure 1: Michelson interferometer

where E_{Arm1} and E_{Arm2} are the interfering optical fields, I_d is the intensity at the detector and I_{Arm1} and I_{Arm2} are the mean intensities of the interfering beams. The second term in the equation, known as the normalized autocorrelation function,[13] represents the amplitude of the intensity variation observed at the detector. This term is dependent on the optical path difference τ between the two arms of the interferometer. In the case of a highly coherent light source such as a laser, the variation of the resultant intensity as a function of path length difference is sinusoidal, as depicted in the upper left of Fig. 1. However, as the degree of coherence decreases the amplitude of the intensity variation decreases, and intensity variation is only observed when the path lengths of the two arms are closely matched, i.e., τ is close to zero. The intensity variation as a function of path length difference then assumes the form shown in the lower left portion of Fig. 1. No variation in the intensity is observed when the path length difference is large. The amplitude of the variation of the intensity increases as the path length difference becomes smaller and a maximum occurs when the path lengths are exactly equal, i.e., τ=0. In other words, the intensity variation observed at the detector is modulated by an envelope function, the width of which is determined by the coherence of the source.

Figure 2 shows the two wave packets produced by reflection from the two surfaces of a transparent sample, one from Surface 1 and the other from Surface 2. The second wave packet is delayed with respect to the first packet by the optical path length (OPL). The optical path length (OPL) of a sample can be expressed by

Downloaded From: https://www.spiedigitallibrary.org/conference-proceedings-of-spie on 10 Apr 2020
Terms of Use: https://www.spiedigitallibrary.org/terms-of-use

$$OPL = \frac{2tc}{v_g} \tag{2}$$

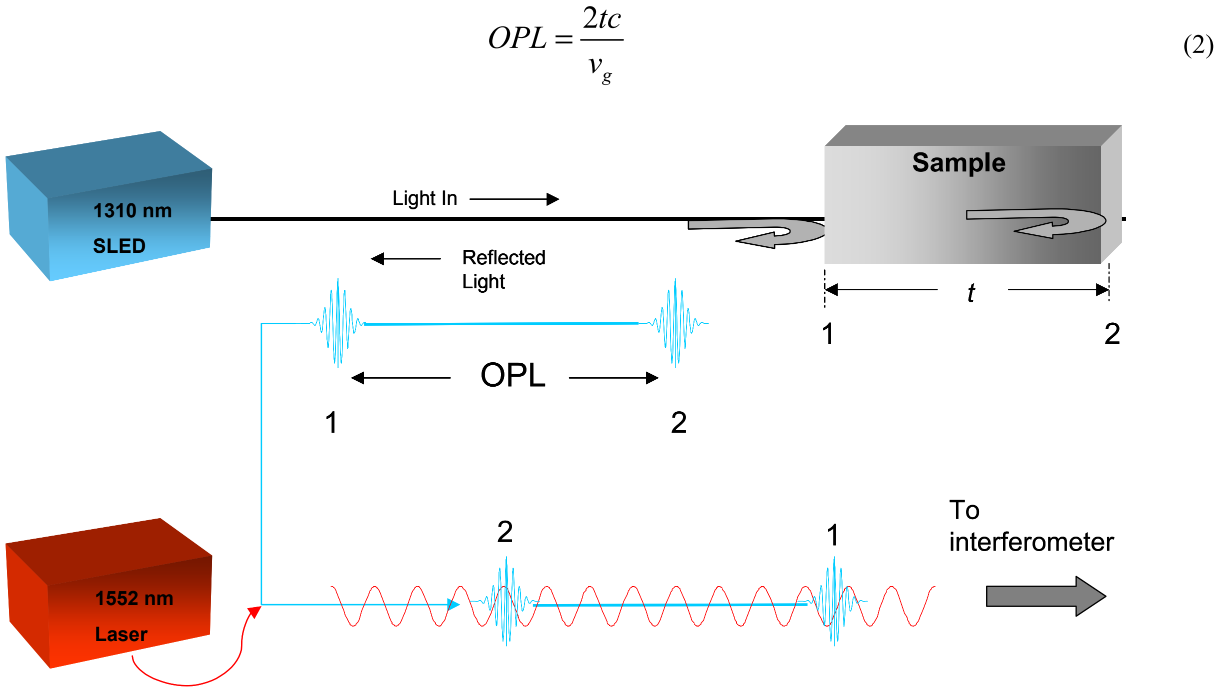

Figure 2: Block diagram showing the light propagation after interaction with sample

where t is the physical thickness of the sample, c is the speed of light in vacuum, and v_g is the group velocity of the wave packet. Group velocity is defined as $\partial\omega/\partial k$, the differential change in angular frequency, ω, as a function of wave number, k. It can be shown that in a dispersive medium the group velocity becomes

$$v_g = v_p \left(1 - \frac{k}{n_p} \frac{\partial n_p}{\partial k} \right) \tag{3}$$

where v_p is the phase velocity and n_p the phase index. It then becomes convenient to define group index, n_g, as

$$n_g = n_p - \lambda \frac{\partial n_p}{\partial \lambda} = \frac{c}{v_g} \tag{4}$$

such that, using Equations (2) and (4), the OPL can be expressed as

$$OPL = 2t \cdot n_g \tag{5}$$

The two reflected wave packets are co-propagated with light from the coherent source and then inputted into the interferometer.

Figure 3 is a block diagram of a bulk-optic equivalent of the all-fiber interferometer. The interferograms resulting from the autocorrelation of the input signals performed by the interferometer are shown in the figure. The autocorrelation is performed by generating two identical copies of the incoming signal at the 50/50 beamsplitter. The copies travel into the two arms of the interferometer, are reflected from the mirrors and recombine at the beamsplitter to interfere with one another. The difference in optical path length encountered by the two beams is determined by the mismatch in the length of the arms of the interferometer. The arm lengths are adjusted in a periodic fashion by scanning the mirrors in synchronization such that an increase in the arm length in one arm is accompanied by a corresponding decrease in the other arm. The low-coherence autocorrelation shows three peaks, a result of three distinct configurations of the scanning

Downloaded From: https://www.spiedigitallibrary.org/conference-proceedings-of-spie on 10 Apr 2020
Terms of Use: https://www.spiedigitallibrary.org/terms-of-use

mirrors. The center lobe occurs when the arms of the interferometer are of equal path length. In this condition, the reflected wave packets from the sample interfere with themselves after propagating through the interferometer (i.e. wave packet 1 from Arm 1 interferes with packet 1 from Arm 2 and wave packet 2 from Arm 1 interferes with packet 2 from Arm 2). As the arms are scanned and the path length in the arms of the interferometer becomes mismatched, the fringe visibility decreases due to the low-coherence of the source. It eventually reaches zero and remains there until the path length change equals the OPL of the sample. When this occurs, another fringe visibility peak is detected as a side lobe. This condition is achieved in two distinct configurations of the interferometer, each of which gives rise to a side lobe. This condition is achieved when wave packet 1 from Arm 1 interferes with wave packet 2 from Arm 2 and vice-versa. When viewed as a function of interferometer path length mismatch, the two side-lobes appear on either side of the central lobe as shown in the figure below.

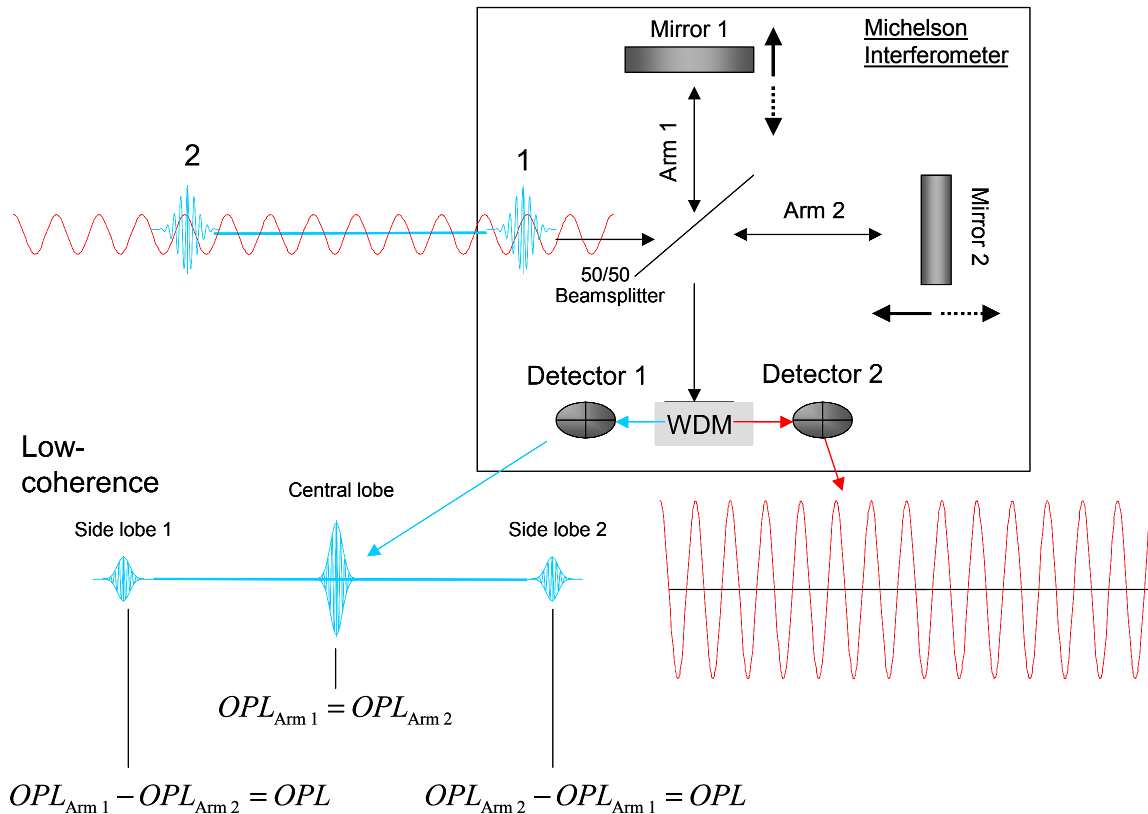

Figure 3: Autocorrelation of the two light source signals

The side lobes are produced when the following condition is met:

$$\left| OPL_{\text{Arm 1}} - OPL_{\text{Arm 2}} \right| = OPL \tag{6}$$

Therefore, the distance from the center peak to either side lobe is the OPL of the sample.

It is evident that to measure the OPL of the sample accurately, it is necessary to determine the path length change accurately in the interferometer as it is scanning. The interferometric signal produced by the coherent source (which is co-propagated into the arms of the interferometer) is used for this purpose. Co-propagation ensures that the optical path length change imparted to the low-coherence signal is measured accurately. Simultaneous measurement of the intensity of the low-coherence signal and the path length change as measured by the coherent signal results in a determination of

Downloaded From: https://www.spiedigitallibrary.org/conference-proceedings-of-spie on 10 Apr 2020
Terms of Use: https://www.spiedigitallibrary.org/terms-of-use

intensity as a function of path length change. This data is then processed in the software and the sample OPL is extracted, as described below.

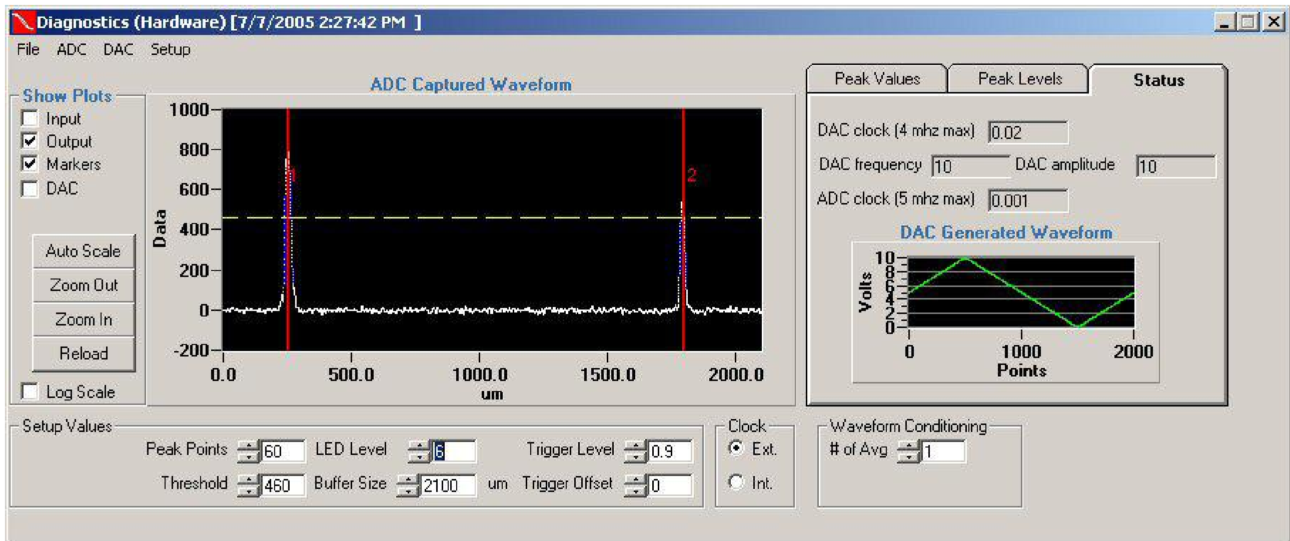

Figure 4: Screen capture of software interface

Figure 4 shows a screen capture of the signal display in the interferometer software. The sample under test is a typical microscope slide approximately 1 mm in thickness. The center peak of the autocorrelation (left peak in figure) and one side lobe are displayed. The software algorithm determines the locations of the intensity envelope maxima. The software then calculates the distance between these peaks and displays it as the OPL (on a separate screen - not shown). Each discrete data point of the signal is spaced at one clock pulse.

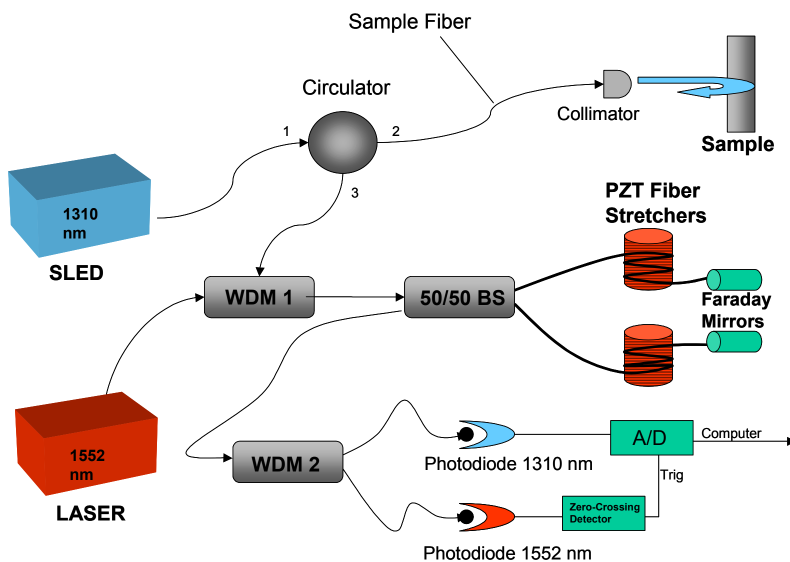

Figure 5: Layout of low-coherence interferometer as an autocorrelator

2.2. Dual Interferometer Layout

The layout of the interferometer is shown in Fig. 5. The light source is a fiber-coupled superluminescent light emitting diode (SLED) operating at a center wavelength of 1310 nm with a bandwidth of 50 nm. The light is sent to the sample through Port 1 and Port 2 of an optical circulator (an optical circulator is a non-reciprocal device that redirects light from port-to-port sequentially in only one direction). The light from Port 2 passes though the sample fiber and a collimator and is incident upon the sample. The reflected light from the sample re-enters the fiber and exits through Port 3 of the circulator. The reflected light from the sample is then combined with the coherent diode laser operating at 1552.52 nm via a wavelength division multiplexer (WDM 1 in the figure). Two copies of the signals at the two wavelengths are produced by a fused-fiber 50/50 splitter and sent into the two arms of the scanning interferometer.

Downloaded From: https://www.spiedigitallibrary.org/conference-proceedings-of-spie on 10 Apr 2020
Terms of Use: https://www.spiedigitallibrary.org/terms-of-use

PZT fiber stretchers are used for the path length scanning of the interferometer. These fiber stretchers are approximately 10 meters of single-mode fiber wrapped around a piezoelectric ceramic cylinder. Applying a high voltage waveform to the piezoelectric crystal changes the physical dimension of the PZT crystal, which in turn causes optical path length changes within the fiber. At full voltage, each PZT can "stretch" the fiber up to 4.5 mm, corresponding to approximately 6.5 mm of optical path length change. Two fiber stretchers, one in each arm of the interferometer, operate in a “push-pull” configuration. The voltage waveform to one PZT is 180° out of phase with the waveform to the other. Depending on the relative path-length of each arm, the interferometer can perform two optical scans per voltage scan or scan twice the optical stretch. In this latter mode of increased stretch, the path length change can be doubled to approximately 13 mm of optical path length thereby enabling the measurement of thicker samples.

Light that exits the fiber stretchers is reflected back into the stretchers by the Faraday mirrors for a second pass through the stretchers (Faraday mirrors are passive devices that reflect light with a polarization rotation change of 90° relative to the input light, independent of the initial polarization state). In order to maximize the fringe visibility of the interferometric signal, the polarization states of the returning beams must be identical. It has been shown that fiber-optic stretchers induce static and dynamic birefringence which corrupt the polarization states.[12] The Faraday mirrors help maximize fringe visibility by performing phase conjugation to compensate for dynamic-bending induced birefringence in the fiber stretchers. The static birefringence is reduced by the canceling effect of matched stretchers in each arm.

The light exits the interferometer through the 50/50 splitter. The two interferometric signals, one produced by the SLED and the other produced by the laser, are separated by a WDM (WDM 2 in the figure). The fringe signals from the SLED and the laser are detected by different photodiodes. The signal generated by the laser is processed by a zero-crossing detection circuit which produces pulses that are used to “clock” the analog-to-digital (A/D) conversion of the signal generated by the low-coherence source. Once the low-coherence fringe signal is digitized, it is demodulated in software and the optical thickness is calculated and displayed in real time.

The primary difference between this layout and other configurations is that this interferometer is set-up as an autocorrelator, i.e. the signal from the sample is split and sent through each arm of the interferometer and recombined to compare the function against itself, effectively determining the autocorrelation function of the signal. In a standard Michelson interferometer configuration, the signal from the sample is sent down one arm of the interferometer while the other arm serves as the reference/scanning arm. The optical autocorrelator configuration has the following advantages.

- The sample fiber is not part of the interferometer. Any changes in OPL are common mode and affect both wave packets equally. Therefore, the length of that fiber is not critical to the operation of the interferometer and precise path length matching is not necessary. The sample then does not need to be local to the interferometer. Since standard single mode fiber is used, distances of kilometers between sample and interferometer are possible.

- Multiple probes can be connected to the same interferometer system. By using a telecom optical switch multiple probes can be read sequentially. This allows one interferometer to read many separate samples or several points on a single sample.[10] This is extremely useful in a production or quality assurance application where a large number of parts require rapid throughput.

3. EXPERIMENTAL EVALUATION

This section describes the experimental evaluation of the instrument performance. A detailed description of the construction of the special artifacts is provided along with a description of the measurement procedure and results.

3.1. Construction of measurement artifacts

As is evident from the foregoing discussion, the interferometer system under test does not measure distance directly. Instead, it measures the optical path length difference between the beam paths traversed by the two reflected beams. This measured difference is the optical path length (OPL) associated with the artifact. The relationship between the OPL and the sample thickness t is given by Equation (5). The physical separation t between the two surfaces is then obtained

Downloaded From: https://www.spiedigitallibrary.org/conference-proceedings-of-spie on 10 Apr 2020
Terms of Use: https://www.spiedigitallibrary.org/terms-of-use

from knowledge of the group index n_g (Equation (4)) of the material in the cavity bounded by the two surfaces (assuming constant index along the beam path) and is given by

$$t = \frac{OPL}{2n_g} \tag{7}$$

The factor of two in the denominator accounts for the two traverses of the length of the artifact by the beam reflected from the second surface.

In light of the fact that the instrument measures OPL, in order to test the instrument, special artifacts that represent a known OPL are required. However, appropriate standards (i.e., optical path length standards) are unavailable and need to be specially constructed for this evaluation. Rearranging Equation (7), it is evident that the desired OPL is simply the product of the physical length t and the index n_g. In order to minimize the uncertainty associated with the standard, uncertainties in both the physical thickness and the group index have to be minimized. An artifact based on an air-gap is chosen because the uncertainty associated with the determination of the index of air is considerably lower than that of most transparent solids. For air, with $n_g \approx 1$, the OPL is very nearly equal to twice the physical path length. A schematic of the artifact is shown in Fig. 4. The accompanying photograph (Fig. 5) shows a close-up of the artifact. The artifacts consist of a square gage block with a hole through the center with two optical flats wrung to the gauging faces of the block. The measurement beam from the interferometer passes through the hole in the gage block. The physical thickness that defines the OPL of interest is the length of the beam path traversed by the measurement beam between the surfaces of the optical flats in contact with the gage block.

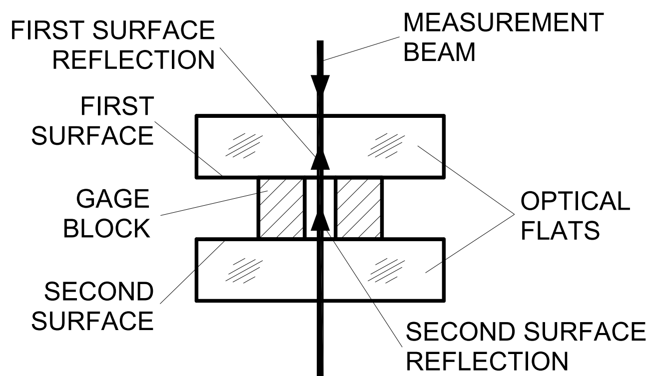

Figure 4: Schematic of OPL artifact

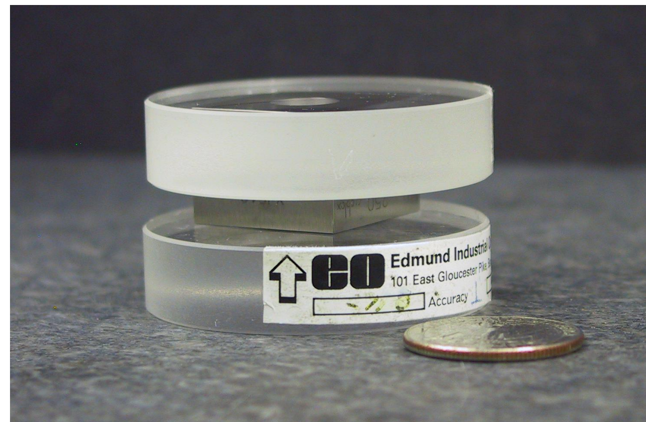

Figure 5: Photograph of assembled artifact

The artifacts are constructed by sequentially wringing the two flats to the gauging faces of the gage block. Eight Starrett-Webber croblox® square gage blocks ranging in size from 0.050 in. to 0.40 in. gage blocks are chosen for this evaluation. The block sizes are chosen to span a substantial portion of the measurement range of the instrument (approximately 0.45 in.). Six of the blocks (0.050 in. to 0.2 in.) are B89.1.9 Grade 00 (GGG-G-15C Grade 1) blocks with the remainder being B89.1.9 Grade 0 (GGG-G-15C Grade 2) blocks. Each of the artifacts is constructed using a single block, i.e., block stacks are avoided to minimize the number of interfaces and the associated uncertainty. The optical flats are 2 in. diameter $\lambda/10$ fused silica flats. Fused silica is chosen for its hardness, thermal and temporal stability and resistance to scratching. The same pair of flats is used for all of the artifacts. The gage blocks and flats used in this evaluation are purchased new and used expressly for this evaluation - this ensures a high-quality wring and minimizes the chances of nicks and burrs on the wringing surfaces affecting the measurement.

The wringing procedure is preceded by a thorough cleaning of the surfaces of both the block and the optical flats with reagent-grade acetone and lint-free optical wipes. The wringing procedure is performed under a monochromatic light source. Multiple fringes (resulting from interference between light reflected from the surface of the flat and the block) are observed when the optical flat and the block are initially brought into contact. A good quality wring is ensured by manipulating the block and the flat until the fringes disappear and a uniform intensity pattern, i.e., a single, fully-fluffed

Downloaded From: https://www.spiedigitallibrary.org/conference-proceedings-of-spie on 10 Apr 2020
Terms of Use: https://www.spiedigitallibrary.org/terms-of-use

fringe, is observed over the entire contact area. A minute quantity of light oil (Starrett M1) is applied to facilitate the wring.

3.2. Experimental method

The artifacts described in the previous section are measured using the setup shown in the schematic of Fig. 6 and the photograph of Fig. 7. The measurement beam exits the system via a fiber and collimator (Fig. 3). The beam is directed along the z-axis of the coordinate system shown in Fig. 6. A collimated beam of diameter 1 mm with a beam waist at approximately 20 mm from the front face of the collimator emerges from the collimator. The collimator position along the z-axis is adjusted such that the beam waist is positioned approximately at the center of the air-gap. The collimator assembly is mounted on a tip-tilt stage, which provides rotation about the x and y axes to facilitate angular alignment (positive x is perpendicular to the plane of the paper and towards the reader). This stage is used only during initial setup to align the collimated beam and is not adjusted during measurement. The measurement beam is directed downwards onto the artifact. The artifact is placed on a tip-tilt stage (Newport Model PO80N) mounted to a pair of linear slides that provide orthogonal linear motion. These four degrees-of-freedom (two angular motions about and two translations along the x and y axes) are used to facilitate alignment of the artifact to the measurement beam. The table of the lower tip-tilt mount is fitted with two shoulder screws that serve as locating points that bear against the edge of the lower optical flat. These locating points facilitate removal and replacement of the sample in a repeatable manner. The lower optical flat also carries an index mark that establishes its azimuthal orientation (angular orientation about the z axis) relative to a fiducial (not shown) on the table of the tip-tilt mount.

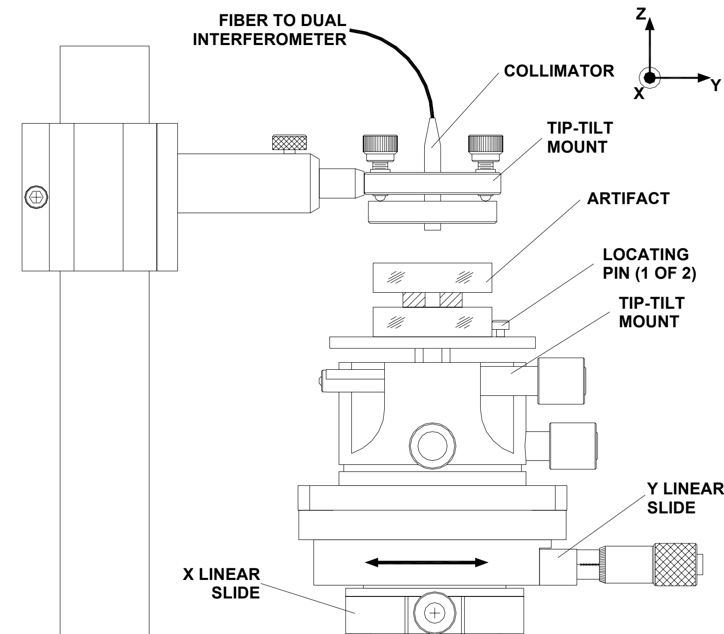

Figure 6: Schematic of test setup

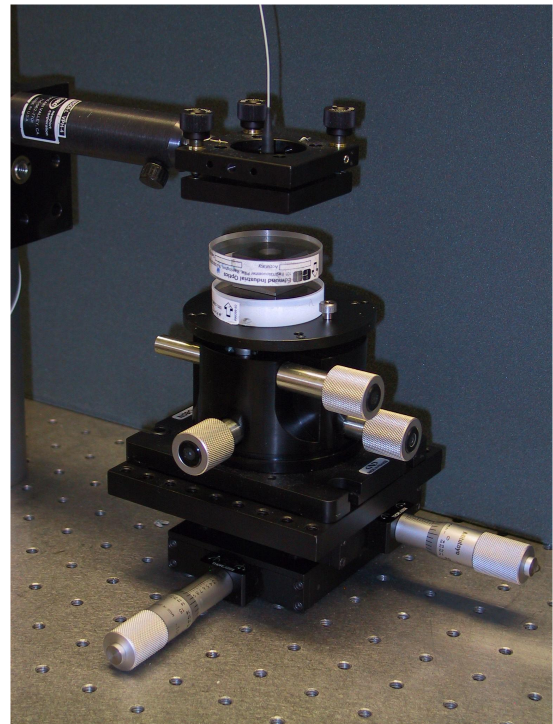

Figure 7: Photograph of test setup

Artifact alignment is performed using the beam from the collimator as an aid. The measurement beam has a wavelength of 1310 nm and as such is invisible to the unaided eye. Alignment is facilitated by disconnecting the input fiber to the collimator from the system and connecting it to a portable diode laser source (Fiber Instrument Sales FDD 111), which produces a red visible beam. This beam is used to perform rough alignment.

Rough alignment is achieved by mounting a mask, consisting of white card with a small aperture (~0.25 mm), at the output of the collimator. The mask is adjusted such that the alignment beam passes through the aperture. The sample is located against the two locating points and positioned in translation using the two linear stages such that the

Downloaded From: https://www.spiedigitallibrary.org/conference-proceedings-of-spie on 10 Apr 2020
Terms of Use: https://www.spiedigitallibrary.org/terms-of-use

measurement beam passes through the center of the hole in the gage block. Four spots formed by beams reflected from each of the surfaces of the flats are observed on the surface of the card. Two of the spots originate from reflections from the surfaces of the optical flat in contact with the gage block, while two others originate from the free surfaces of the top and bottom flat. The latter two spots are displaced from the first two spots due to the intentional wedge between the surfaces of each optical flat. The angular orientation of the sample about the x and y axes is then adjusted by manipulating the lower tip-tilt stage until the two reflections from the wrung surfaces coincide with one another and the aperture in the card. A final check is made to ensure that the beam passes through the center of the hole in the gage block and adjustments are made with the linear stages if required. Alignment of the beam with the center of the hole is determined by moving one of the linear stages until the beam just grazes the edge of the hole. The position of the stage is recorded and the sample is then translated until the beam grazes the other edge of the hole, approximately diametrically across from the previous position. The stage is then moved to a position midway between these two positions. The procedure is repeated with the other slide to ensure alignment in the orthogonal direction. The position of the sample is refined by repeating this adjustment. The card is then removed and the input fiber to the collimator reconnected.

Fine alignment is performed with the aid of the measurement beam. Minor adjustments are made to the tip-tilt stage until the beams from the two surfaces are retroreflected into the collimator and thence into the fiber. The intensity of the two return beams is a sensitive function of angular alignment and is displayed by the control software as an alignment aid. Alignment is optimized by maximizing the observed signal strength of the two beams and minimizing the measured OPL value. The relatively high-speed performance of the instrument facilitates the quasi real-time monitoring of the measured OPL and the beam intensities, thus providing feedback for alignment. Angular misalignments of approximately ±0.17° result in extinction of the return beam and complete loss of signal. In practice, the sample can be aligned to the beam to better than 0.05°.

Data is sampled at rates varying from of 10 Hz for the smaller artifacts to 2 Hz for the larger artifacts, with sampling windows varying from approximately 60 sec to 80 sec respectively. The average of the acquired data is computed and constitutes a single reading. The temperature of the ambient air is measured in the vicinity of the gage block. The temperature of the block is assumed to be the same as that of the air. This assumption is verified in the case of the larger blocks, for which the spacing between the flats permits a banjo-type thermistor (YSI 440) to be inserted into the gap and into contact with the block. The thermistor is monitored using a Omega Model HH42 digital thermometer. The calibration of the thermometer is checked against a Hart Scientific Model 1529 secondary reference thermometer equipped with Hart Scientific 5611 thermistor probes. The ambient air pressure is measured using a Druck DPI 145 and a RPT 200-1676 pressure transducer located in close proximity to the artifact. Humidity is recorded but not used in the calculation of the refractive index (see Section 4.3). The assumption is made that these measurements are representative of the environmental conditions prevalent within the enclosed cavity between the optical flats.

4. EVALUATION OF INSTRUMENT PERFORMANCE

This section describes the methods and procedures used to estimate the error and the uncertainty associated with the error. This description includes the development of the mathematical model of the measurement, a detailed description of the procedure used to estimate the uncertainty associated with the artifacts, and a determination of the measurement error and its uncertainty.

4.1. Overview of the method of uncertainty estimation

The aim of this exercise is to obtain an estimate of the 'out-of-the-box' performance of the instrument. The approach used here is based on the measurement of a number of artifacts or standards that simulate known values of the measurand. The difference between the values obtained from the instrument and the values established for the artifacts is the measurement error and is one measure of the instrument performance. However, the significance of the measured error can only be established in the context of the uncertainty associated with the measurement and the uncertainty associated with the established values of the artifacts. While the artifacts are designed so as to relate them in a direct manner to the fundamental standard of length, various other factors must be taken into account to establish an associated uncertainty for each of the artifacts.

Downloaded From: https://www.spiedigitallibrary.org/conference-proceedings-of-spie on 10 Apr 2020
Terms of Use: https://www.spiedigitallibrary.org/terms-of-use

This analysis is divided into two parts. The first presents the mathematical model for the quantity of interest, i.e., the measurement error. This model is used to develop an expression for the uncertainty in the error. Not surprisingly, it will be seen that one of the contributors to the uncertainty of the error is uncertainty associated with the artifacts. The second part presents a treatment for the calculation of this uncertainty.

Typical uncertainty evaluations are based on the methodology outlined in the ISO Guide to Expression of Uncertainty in Measurement (hereafter referred to as the GUM).[14] The first step in a typical GUM-style evaluation involves development of an equation that relates the measurand to the various influence quantities. This equation represents a mathematical model of the measurement and is hereafter referred to as the model equation. The combined standard uncertainty of a measurement or quantity is then estimated by calculating the weighted root-sum-square (RSS) of the uncertainties associated with each of the influence quantities, the weighting factors being the squares of the sensitivity coefficients calculated from the model equation.

4.2. Mathematical model of the measurement

The evaluation of the instrument performance involves the determination of the difference between the measured value and the calibrated value of the reference artifact (the 'error'). The error or deviation so obtained is then assessed within the context of the uncertainty associated with the error. The first step in this process is the development of an expression that relates the measurand to the quantities that influence the measurand, i.e., the influence quantities. The measurand in this case is the error e, which is defined by

$$e = \frac{OPL_{measured} - OPL_{artifact}}{2n_g} \tag{8}$$

where, $OPL_{measured}$ and $OPL_{artifact}$ are the measured value of the OPL reported by the instrument and the calibrated OPL value of the artifact respectively and n_g is the group index of the air in the cavity bounded by the two optical flats. The factor of two in the denominator accounts for the two traverses of the length of the artifact by the beam reflected from the second surface of the artifact. The uncertainty associated with the error may then be calculated using the Law of Propagation of Uncertainty as described in the GUM and given by

$$u_c^2(y) = \sum_{i=1}^{N}\left(\frac{\partial f}{\partial x_i}\right)^2 u^2(x_i) + 2\sum_{i=1}^{N-1}\sum_{j=i+1}^{N}\frac{\partial f}{\partial x_i}\frac{\partial f}{\partial x_j}u(x_i)u(x_j)r(x_i,x_j) \tag{9}$$

The sensitivity coefficients are the partial derivatives in Equation (9) and are obtained by differentiating the model equation (denoted by f) with respect to each of the influence quantities which have an uncertainty (denoted by the standard uncertainty $u(x_i)$) associated with them.

Applying Equation (9) to the model equation (Equation (8)) results in an expression for the uncertainty of the error $u(e)$ that is given by

$$u(e) = \frac{1}{2n_g}\left[\underbrace{u^2(OPL_{measured})}_{\text{Uncertainty in the determination of OPL}} + \underbrace{u^2(OPL_{artifact})}_{\text{Uncertainty associated with artifact OPL}} + \frac{1}{n_g^2}(\Delta OPL)^2 u^2(n_g)\right]^{\frac{1}{2}} \tag{10}$$

where $\Delta OPL = OPL_{measured} - OPL_{artifact}$

Downloaded From: https://www.spiedigitallibrary.org/conference-proceedings-of-spie on 10 Apr 2020
Terms of Use: https://www.spiedigitallibrary.org/terms-of-use

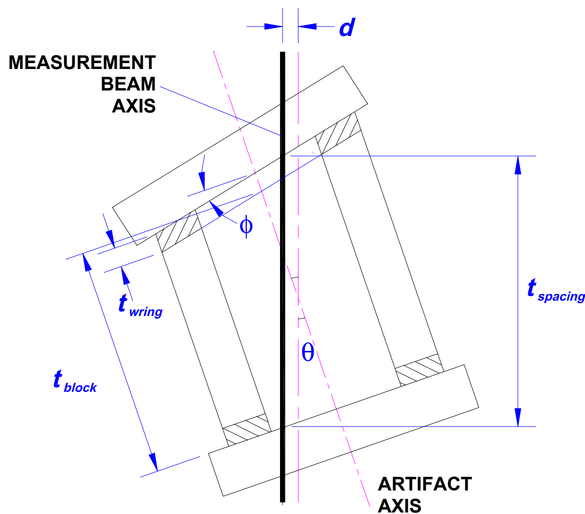

Figure 8: Misaligned artifact

The first term in the above equation is the uncertainty associated with the determination of the OPL. This is estimated by computing the standard deviation of the mean of a number of readings. The second term represents the uncertainty in OPL associated with the measurement artifact. This is akin to the uncertainty associated with the any other calibrated artifact, e.g., a gage block. The final term represents the contribution of the uncertainty in the index of refraction associated with the artifact. It can be seen that for a well-calibrated instrument, the difference between the measured OPL and the OPL of the artifact is small, thereby minimizing the contribution of this term.

The following section describes the calculation of the uncertainty associated with a measurement artifact.

4.3. Estimation of artifact uncertainty

In accordance with the procedures outlined above, the first part of this section describes the derivation of the model equation. The measurand in this case is the OPL, an expression for which may be obtained by rearranging Equation (7) and adding appropriate subscripts to give

$$OPL_{artifact} = 2t_{spacing} \cdot n_g \tag{11}$$

where $t_{spacing}$ is the physical length traversed by the measurement beam and n_g is the average group index along this path in the cavity enclosed by the two optical flats. Another consequence of the fact that this technique measures *group phase* rather than *wave phase*, is that the difference in phase change on reflection at the two surfaces does not influence the measured OPL and is not included in the model equation. This is in contrast to single-wavelength interferometry that measures wave phase.

The relationship between the physical path, $t_{spacing}$, and the sample geometry is illustrated in Fig. 8. This includes the thickness t_{block} of the gage block, non-parallelism ϕ of the surfaces of the optical flats, angular misalignment θ between the axis of the artifact and the measurement beam, lateral displacement d between the measurement axis and the axis of the artifact and the wring film thickness t_{wring}. For small angles, an expression relating these parameters to the physical path length traversed by the beam is given by

$$t_{spacing} = \left(t_{block} + t_{wring}\right) \cdot \left(1 + \frac{1}{2}\theta\left(\theta + \phi\right)\right) + d \cdot \phi \tag{12}$$

Note in the above expression, that although there are two wring films in the artifact, only one of the wring film thicknesses t_{wring} appears. This is due to the fact that the definition of length of a gage block includes the thickness of one wring film and this is reflected in the certified length of the block.

The length of the block is a function of the temperature and can be different from the certified value when measurements are made at a temperature other than that at which the block was calibrated (usually 20 °C). For small excursions from the reference temperature, the length of the block may be expressed in terms of its length at 20 °C (denoted here by t_{20}) by

$$t_{block} = t_{20}\left[1 + \alpha\left(T_m - 20\right)\right] \tag{13}$$

where, T_m is the temperature at which the measurement is made in degrees Celsius and α is the coefficient of thermal expansion (CTE) of the gage block. Substituting Equation (13) in (12) results in a complete expression for $t_{spacing}$ given by

Downloaded From: https://www.spiedigitallibrary.org/conference-proceedings-of-spie on 10 Apr 2020
Terms of Use: https://www.spiedigitallibrary.org/terms-of-use

$$t_{spacing} = \left[t_{20} \left(1 + \alpha \Delta T \right) + t_{wring} \right] \cdot \left[1 + \frac{1}{2} \theta \left(\theta + \phi \right) \right] + d\phi \tag{14}$$

It now remains to calculate the effect of the relevant influence quantities on the group refractive index of the air in the cavity. The group index is a function of the center wavelength, the phase index at this wavelength, and the slope of the dispersion curve, and is given by Equation (4). The phase index n_p for air is given by the corrected Edlén equation due to Birch and Downs[15] given by

$$n_p = 1 + 10^{-8} \left[8342.54 + \frac{2406147}{130 - \sigma^2} + \frac{15998}{38.9 - \sigma^2} \right] \times \left[\frac{P_m}{96095.43} \right] \left[\frac{1 + 10^{-8} \left(0.601 - 0.00972 T_m \right) P_m}{1 + 0.0036610 T_m} \right] + \underbrace{\text{humidity term}}_{Neglected} \tag{15}$$

$$\text{where } \sigma = \frac{1}{\lambda}$$

where λ is the wavelength, P_m is the air pressure and T_m is the air temperature, in units of μm, Pa and °C respectively. The humidity term and the uncertainty associated with the humidity are neglected in this analysis. This is justified by the fact that the sensitivity of the group index to changes in relative humidity is extremely low and of the order of $\sim 1 \times 10^{-8}$/%RH. This suggests that a 10% change in humidity contributes an uncertainty of ~0.1 ppm or 1.25 nm for a air-gap of 12.5 mm. Excluding the term affects the nominal value of the index in a similar fashion with the difference between the index evaluated at ~30%RH and in the absence of the humidity term being ~0.25 ppm which changes the calculated air-gap thickness by ~3.2 nm. Inclusion of the term results in a tremendous increase in the complexity of the calculations without a commensurate increase in their accuracy.

The complete model equation is obtained by substituting Equations (4) and (14) in (11) to give the model equation for the OPL of the artifacts, given by

$$OPL_{artifact} = 2 \cdot \left[\left\{ t_{20} \left(1 + \alpha \Delta T \right) + t_{wring} \right\} \cdot \left\{ 1 + \frac{1}{2} \theta \left(\theta + \phi \right) \right\} + d\phi \right] \cdot \left[n_p - \lambda \frac{\partial n_p}{\partial \lambda} \right] \tag{16}$$

where the phase index n_p for air is given by Equation (15). Equation (16) is the model equation for the artifact uncertainty estimation and serves as the basis for the calculation of the sensitivity coefficients. The uncertainty associated with the OPL of the artifact is determined by application of the Law of Propagation of Uncertainty, which is given by Equation (9).

The sensitivity coefficients so obtained are tabulated in Table 1 along with numerical estimates of the standard uncertainties of the various influence quantities for the case of the artifact with the 10.1 mm (0.4in.) air-gap. Also included are the nominal values that are used in the calculation of the various sensitivity coefficients, the type of uncertainty evaluation and the probability distribution assigned to each of the influence quantities. The sensitivity coefficients vary slightly from artifact to artifact due to the fact that the nominal values for pressure and temperature used in their calculation are slightly different and depend on the values measured at the time of the measurement. The expressions present the sensitivity coefficients in terms of the nominal gap length t_{20} and are included for reference. Table 2 lists the uncertainties associated with all the artifacts along with the uncertainty in the average of the measured OPL and the measured error. The uncertainty in the average $u(OPL_{measured})$ is calculated according to the recommendations of the GUM and is given by

$$u(OPL_{measured}) = \frac{\sigma(OPL_{measured})}{\sqrt{N}} \tag{17}$$

where $\sigma(OPL_{measured})$ is the standard deviation of the measured data and N is the number of data points used to compute the average.

Downloaded From: https://www.spiedigitallibrary.org/conference-proceedings-of-spie on 10 Apr 2020
Terms of Use: https://www.spiedigitallibrary.org/terms-of-use

Table 1: Influence quantities, sensitivity coefficients and uncertainties associated with 10.1 mm (0.4 in.) air-gap artifact

S. No.	Influence Quantity	Nominal Value	Units	Sensitivity Coefficient $c_i = \left(\partial f / \partial x_i\right)$	Magnitude of Sensitivity Coefficient $\lvert c_i \rvert$	Uncertainty Evaluation Type	Assumed Distribution	Standard Uncertainty $u(x_i)$	$\left(\partial f / \partial x_i\right)^2 u^2(x_i)$
1	t_{20}	10159.97	µm	2.006	2.0	Type B	Normal	0.025	2.5×10^{-3}
2	T_m	20.75	°C	$-21.2\times10^{-9}+15.2\times10^{-6}t_{20}$	154×10^{-3}	Type B	Uniform	0.3	2.13×10^{-3}
3	P_m	101.24×10^3	Pa	$10^{-9}\left(0.06+5.3t_{20}\right)$	54.2×10^{-6}	Type B	Uniform	400	4.70×10^{-4}
4	t_{wring}	0.010	µm	2.006	2.0	Type B	Uniform	0.009	3.24×10^{-4}
5	θ	0.87×10^{-3}	radians	$17.4\times10^{-6}\left(1+10^2 t_{20}\right)$	17.75	Type B	Uniform	0.87×10^{-3}	2.38×10^{-4}
6	α	8.5×10^{-6}	K^{-1}	$1.5t_{20}$	15.2×10^3	Type B	Uniform	0.5×10^{-6}	5.78×10^{-5}
7	d	1	mm	3×10^{-3}	3×10^{-3}	Type B	N/A	1	9.0×10^{-6}
8	ϕ	1.5×10^{-6}	radians	$2000.5+0.87\times10^{-3}t_{20}$	2×10^3	Type A	Normal	1.2×10^{-6}	5.76×10^{-6}
9	λ	1.300	µm	$-\left(95.8\times10^{-9}+8.3\times10^{-6}t_{20}\right)$	84.63×10^{-3}	Type B	Uniform	0.009	5.80×10^{-7}
where t_{20} is in units of µm					$u_c\left(OPL_{artifact}\right) = \left[\sum_{i=1}^{N}\left(\partial f / \partial x_i\right)^2 u^2(x_i)\right]^{\frac{1}{2}}$				**0.076 µm**
					Expanded Uncertainty $U = 2u_c\left(OPL_{artifact}\right)$				**0.152 µm**

The same data is presented graphically in Fig. 9, with the error bars representing the expanded uncertainty with a coverage factor of two. The following sections provide a brief justification for the nominal values and the standard uncertainties chosen for each of the influence quantities.

4.3.1 Temperature T_m and pressure P_m

Temperature T_m influences both the length of the gage block and the group index of refraction. The nominal value of temperature used in the uncertainty calculation is the temperature recorded at the time of measurement of the artifact. A maximum of 0.5 °C is assigned to the temperature. This value is arrived at on the basis of a Type B evaluation and

Downloaded From: https://www.spiedigitallibrary.org/conference-proceedings-of-spie on 10 Apr 2020
Terms of Use: https://www.spiedigitallibrary.org/terms-of-use

Table 2: Error, uncertainty associated with artifacts resulting uncertainty in the error

S. No.	Nominal Air-gap (mm)	Error [per Eq. (8)] (nm)	$u_c(OPL_{measured})$ (nm)	$u_c(OPL_{artifact})$ (nm)	$u_c(e)$ (nm)	$U(e)=2u_c(e)$ (nm)
1	1.27	39.4	4.7	53.7	27.0	53.9
2	1.59	75.7	4.6	54.0	27.1	54.1
3	2.54	22.5	4.6	55.0	27.6	55.1
4	3.18	60.4	4.6	55.9	28.0	56.0
5	3.81	76.0	6.4	57.0	28.7	57.3
6	5.08	151.8	6.4	59.7	30.0	60.1
7	7.62	250.9	9.7	66.9	33.8	67.6
8	10.16	306.8	8.8	75.8	38.1	76.3

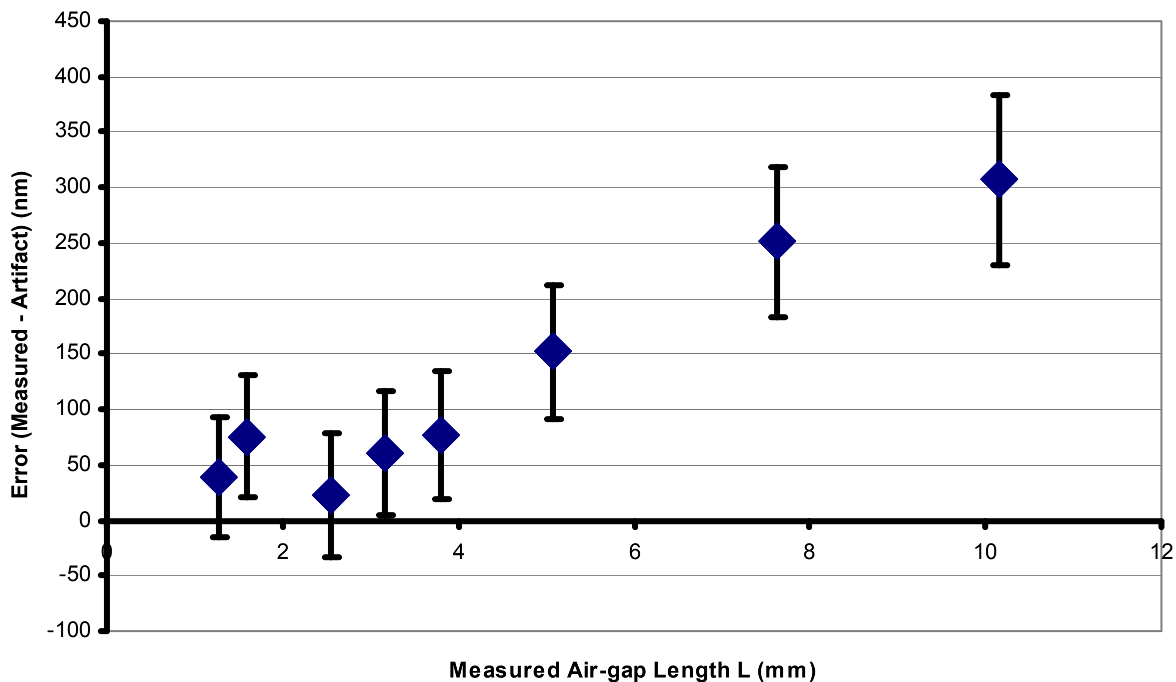

Figure 9: Error and the uncertainty in the error

includes the contributions due to the measurement uncertainty associated with the thermometer and the contributions of any gradients. This quantity is assumed to have uniform probability distribution, i.e., the temperature is assumed to be characterized by a rectangular distribution with a half-width a=0.5 °C. The standard uncertainty in the temperature is then given by[14]

$$u(T_m) = \frac{a}{\sqrt{3}} \cong 0.3\,^0\mathrm{C} \qquad (18)$$

Downloaded From: https://www.spiedigitallibrary.org/conference-proceedings-of-spie on 10 Apr 2020
Terms of Use: https://www.spiedigitallibrary.org/terms-of-use

The pressure P_m is treated similarly and the knowledge of the pressure is assumed to be represented by a uniform distribution with a half-width of 5 mm Hg based on a Type B evaluation. This value takes into consideration the measurement uncertainty associated with the barometer and contributions due to gradients. The standard uncertainty, calculated using an expression analogous to Equation (18), is 3 mm Hg.

The pressure also affects the length of the gage block due to hydrostatic compression. This effect, however, is extremely small and has been ignored in this treatment. Further, while the effects of the uncertainty in the determination of pressure and temperature on the index of refraction have been taken into account in this analysis, the uncertainty associated with the Edlén equation has been neglected. The standard uncertainty associated with the equation[15] is $\sim 1 \times 10^{-8}$. This corresponds to an uncertainty in the measured length of ~ 125 pm, which may be neglected for this evaluation.

4.3.2. Block length t_{20} and wring film thickness t_{wring}

The nominal value for the block thickness at 20 °C is obtained from the calibration certificate for the block. The value is calculated by adding a deviation value to the nominal value of the block. For a square gage block five deviation values are specified. The deviations are measured at four auxiliary points around the central hole and at a so-called 'reference point.' The average value of the deviations at the auxiliary points is used in these calculations rather than the deviation at the reference point. It is felt that this average value better represents the length of the block in the region of the hole than the value represented by the measurement at the reference point. The uncertainty associated with t_{20} is obtained directly from the calibration certificate of the block and constitutes a Type B determination. A normal distribution is assigned to the block thickness so that the standard uncertainty is one-half of the k=2 expanded uncertainty reported on the calibration certificate.

The nominal value of the wring-film is taken from the literature[16] and is assumed to be 0.010 µm. The uncertainty in the wring film thickness is based on the variation reported in the same source. The uncertainty in the wring-film thickness is assumed to be represented by a uniform distribution with a half-width of 0.015 µm. This value is established from the reported variation in wring film thickness from less than zero to 0.025 µm.[16] The standard uncertainty is calculated from the half-width as before to give 0.0085 µm, which is close to the value reported by Decker and Pekelsky[17] of 0.006 µm.

4.3.3. Thermal expansion coefficient α

The nominal value for the Starrett-Weber croblox® gage blocks is taken from the manufacturers literature.[18] The uncertainty is calculated by adopting the accepted practice of assuming a maximum deviation of 10% from the nominal value or 0.85 ppm K^{-1}. Furthermore, it is assumed in this Type B evaluation that the uncertainty in the expansion coefficient is uniformly distributed with a distribution half-width a = 0.85 ppm K^{-1}. The standard uncertainty is calculated in a manner analogous to that of Equation (18) and is assigned a value of 0.5 ppm K^{-1}.

4.3.4. Artifact angular misalignment θ and lateral displacement *d*

The uncertainty in the alignment of the axis of the artifact to the measurement beam is established based on the behavior of the intensity of the reflected beams and the OPL as measured by the system. As described in 2.2, angular misalignments of approximately ±0.17° result in extinction of the return beam and complete loss of signal. While this value of angular deviation could be used to estimate the uncertainty, it is observed that the sample can be fine-aligned within this range to ~±0.08° by maximizing the intensities of the signal beams. Assigning a uniform distribution to θ results in a Type B standard uncertainty of ~0.05° (0.87 mrad). A nominal value of 0.05° (0.87 mrad) is assumed for θ.

The nominal value and uncertainty of the lateral displacement d are determined by noting that the diameter of the visible alignment beam (see Section 3.2) is ~1 mm. As the positioning of the sample is carried out by monitoring the position of the spot relative to the edge of the hole, it is assumed that the uncertainty in position of the sample can be as large as the beam diameter. Thus, the standard uncertainty is assigned a conservative value of 1 mm. Further, it is assumed that during any given measurement, there can exist a misalignment of 1 mm. A nominal value of 1 mm is used in the uncertainty calculation.

4.3.5. Optical flat parallelism ϕ

Downloaded From: https://www.spiedigitallibrary.org/conference-proceedings-of-spie on 10 Apr 2020
Terms of Use: https://www.spiedigitallibrary.org/terms-of-use

The nominal value of the angle ϕ (Fig. 8) is arrived at by calculating the average non-parallelism in the set of blocks used in this evaluation. The non-parallelism for each block is calculated by computing the maximum variation reported on the gage block certificate (i.e., the maximum difference between deviations reported at the auxiliary points) and dividing that by the separation between auxiliary points oriented on opposite sides of the hole in the block. This separation is assumed to be 12.7 mm (0.5 inches). The resulting average value (over eight blocks) is 1.5 μrad with a standard deviation of 1.2 μrad. The latter value is used as the standard uncertainty from this Type A evaluation. This result was further confirmed by autocollimator measurements of the angle between the two flats. No angular deviation could be detected with the autocollimator, to a resolution of is ~2.5 μradians.

4.3.6. Center wavelength λ

The nominal value of the center wavelength of the broadband superluminescent laser diode source is taken directly from the measured value reported on the manufacturer's certificate accompanying each diode. Although the nominal wavelength for this type of diode is 1310 nm, the manufacturer's measured value for the particular diode in the unit under test of 1300 nm is adopted as the nominal center wavelength. Further, while the uncertainty of the manufacturers measurement is unknown, the manufacturer reports that center wavelength for this class of diode can range from 1290-1320 nm. In this particular case, the bounds are not symmetric with respect to the best estimate. This suggests that the probability of distribution of the wavelength is not uniform throughout. However, absent any other information, the standard uncertainty can be calculated by assuming the probability distribution to be rectangular with upper and lower bounds b_+ and b_-. The standard uncertainty in the wavelength $u(\lambda)$ is then given by

$$u(\lambda) = \frac{(b_+ - b_-)}{\sqrt{12}} \cong 9 \text{ nm} \quad (19)$$

5. DISCUSSION OF RESULTS

Several features of the graph in Fig. 9 and the data in Table 2 merit discussion:

- The combined expanded uncertainty increases with air-gap size. This is consistent with expectations and is primarily driven by thermal effects. This conclusion is consistent with the fact that the contribution due to thermal effects is one of the primary sources of uncertainty (the uncertainty associated with the length of the block being the other) and that this uncertainty contribution is proportional to the length of the block.
- It is apparent from the graph in Fig. 9 that there is a systematic effect as evidenced by the gradual increase in the error with air-gap dimension. Further, it is also evident that the error is larger that the combined expanded uncertainty. This suggests that the trend is real.
- This graph also suggests that the instrument may be error mapped by fitting a suitable function to the data.
- Analysis of the data in Table 2 suggests that the main contributor to the uncertainty is the uncertainty associated with the artifacts. The uncertainty in the average measured value is insignificant in comparison with the uncertainty associated with the artifacts. This suggests that the quality of any mapping is limited by the uncertainty associated with the artifacts. In other words, a better error map may be obtained if artifacts with lower uncertainties are used in the calibration process, the ultimate performance limit being set by the repeatability of the instrument.

As a final exercise, the uncertainty associated with the predicted values from such an error map is calculated. The following procedure is used to fit a function to the data and determine the uncertainty associated with the predicted values:

1. A suitable function is fit to the data that represents the error as a function of the measured thickness. The function chosen in this case is a straight line which is fit to the data in the least-squares sense.
2. The uncertainty in the error, which is the RSS sum of the instrument uncertainty associated with the average value reported by the instrument and the uncertainty associated with the artifact, is used as the uncertainty associated with each data point.

Downloaded From: https://www.spiedigitallibrary.org/conference-proceedings-of-spie on 10 Apr 2020
Terms of Use: https://www.spiedigitallibrary.org/terms-of-use

3. The uncertainty in the error is propagated through to the fit coefficients, i.e., the slope and the intercept of the fit line.
4. The uncertainties in the fit coefficients are used to predict the uncertainty in the error at any arbitrary measured dimension within the range of the instrument.

The above procedure represents a *de facto* calibration of the instrument with this set of measurement artifacts.

The slope and intercept coefficients, as well as their standard uncertainties and correlation coefficient, are calculated using well-known formulae published in texts on data analysis and scientific computing (see for example, Bevington[19], Press *et al*[20]). It should be noted that the least-squares line fit takes the uncertainty associated with each point into account by weighting each data point with its corresponding uncertainty. The calculated values are listed in Table 3.

Table 3: Fit parameters and uncertainties in fit parameters

S. No.	Fit Parameters	Value	Uncertainty
1	Slope m	31.8 nm/mm	$u(m) = 4.07$ nm/mm
2	Intercept c	−18.1 nm	$u(c) = 18.7$ nm

The uncertainty in the predicted values is then calculated by applying Equation (9) to the equation of the line, i.e., $y=mL+c$. It should be noted that the slope m and the intercept c are calculated from a common set of data, and are in general correlated. The effect of this correlation is accounted for by the second term in Equation (9) and requires knowledge of the correlation coefficient $r(m,c)$ between the uncertainties in the slope and intercept. The resulting equation for the standard uncertainty in the predicted error $u(e_p)$ is given by

$$\begin{aligned} u\left(e_p\right) &= \left[u^2\left(m\right)L^2 + u^2\left(c\right) + 2Lu\left(m\right)u\left(c\right)r\left(m,c\right)\right]^{\frac{1}{2}} \\ &= \sqrt{16.64x^2 - 126.83x + 350.96} \end{aligned} \quad (20)$$

where L is any arbitrary air-gap in mm within the range of the instrument, with $r(m,c)$=-0.830. A plot of expanded uncertainty (k=2) based on this expression as a function of air-gap length in mm is shown in Fig. 10.

The somewhat cumbersome expression of Equation (20) may be replaced by simpler linear equation by calculating the equation of an enveloping straight line that is everywhere greater than the computed uncertainty value. This is represents a much more conservative estimate of the uncertainty and is represented by the straight line Fig. 10. The predicted expanded uncertainty as represented by this linear function is given by

$$u\left(e_p\right) = \left(2.9L + 37.5\right) \text{ nm} \quad (21)$$

where the air-gap length L is in mm.

6. CONCLUSIONS

The performance of the dual-interferometer system is evaluated by comparison to specially constructed artifacts. The first part of this evaluation is used to determine the 'out-of-the-box,' i.e., uncalibrated, performance of the instrument. The instrument performance is evaluated in the context of the artifact uncertainties and the measurement variability. A detailed uncertainty analysis for the uncertainty associated with the artifact OPL is presented, from which it is evident that the uncertainty in the error is dominated by the artifact uncertainties. The largest error of ~310 nm was observed in the case of the 10.1 mm air-gap, a relative error of 30 ppm. Further, it is observed that the there appears to be a systematic dependence of the error on the air-gap length (Fig. 9). This suggests that the instrument performance can be improved by error mapping. A simple linear fit is performed in the latter part of this paper and the uncertainties of the fit coefficients are calculated based on the uncertainty in the error. These uncertainties in the fit coefficients are then used to predict the uncertainty associated with the error after mapping. A simplified expression (Equation (21) is derived which suggests that the maximum uncertainty in the predicted error (k=2) is ~75 nm.

The uncertainty in the predicted error is driven by the uncertainty associated with the error. The bulk of the uncertainty in the error is due to the measurement artifacts, with the uncertainty associated with the measured OPL being almost an

Downloaded From: https://www.spiedigitallibrary.org/conference-proceedings-of-spie on 10 Apr 2020
Terms of Use: https://www.spiedigitallibrary.org/terms-of-use

order of magnitude smaller. This suggests that lower uncertainties in the predicted error can be established provided artifacts with commensurately lower uncertainties can be constructed. The ultimate limit on the instrument performance is, of course, imposed by the uncertainty in the determination of the OPL. However, reductions in the uncertainty of the predicted error can be envisaged until the uncertainty associated with the artifacts becomes comparable to the uncertainty associated with the determination of the OPL.

7. ACKNOWLEDGMENTS

The authors would like to express their thanks to Dr. W. Tyler Estler of NIST for his guidance and for reviewing the manuscript.

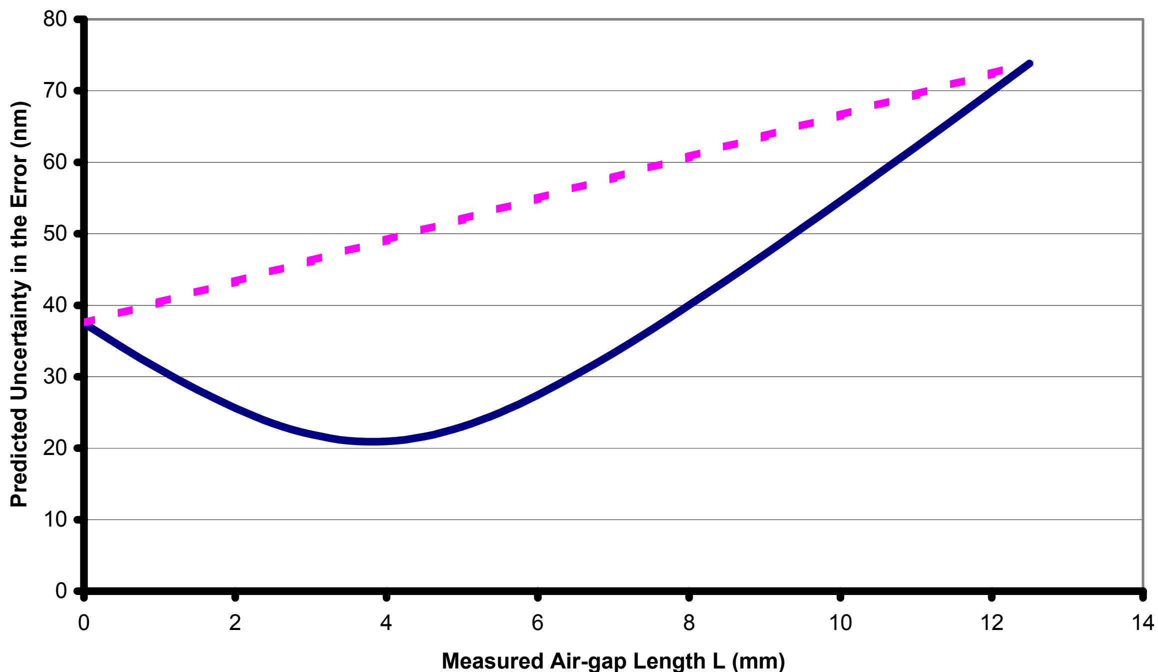

Figure 10: Predicted uncertainty for any arbitrary air-gap length (k=2)

REFERENCES

1. S. Yokoyama *et al.*, "Real-time and high-resolution absolute-distance measurement using a two-wavelength superheterodyne interferometer," *Meas. Sci. Technol.*, **10**(1999), pp. 1233-1239.
2. A. Hirai and H. Matsumoto, "Low-coherence tandem interferometer for remote calibration of gauge blocks," *Proc. SPIE*, Vol. 5190, 2003.
3. D. M. Baney and W. V. Sorin, "Extended-Range Optical Low-Coherence Reflectometry Using a Recirculating Delay Technique," Instruments and Photonics Laboratory, HPL-93-93, April 1993.
4. S. D. Dyer, K. B. Rochford, and A. H. Rose, "Fast and accurate low-coherence interferometric measurements of fiber Bragg grating dispersion and reflectance," *Opt. Express*, Vol. 5, No. 11, pp. 262-266, 1999.
5. D. Huang *et al.*, "Optical coherence tomography," *Science*, Vol. 254, pp. 1178-1181, 1991.
6. M. A. Marcus and S. Gross, "Associated Dual Interferometric Measurement Method for Determining a Physical Property of an Object," U.S. Patent #5,596,409, 1997.
7. M. A. Marcus, S. Gross and D. Wideman, "Associated Dual Interferometric Measurement Apparatus for Determining a Physical property of an Object," U.S. Patent #5,659,392, 1997.

Downloaded From: https://www.spiedigitallibrary.org/conference-proceedings-of-spie on 10 Apr 2020
Terms of Use: https://www.spiedigitallibrary.org/terms-of-use

8. M. A. Marcus, J-R Lee, H.W. Harris and R. Kelbe, "Apparatus for Measuring Material Thickness Profiles," U.S. Patent #6,067,161, 2000.
9. M. A. Marcus, J-R Lee, and H.W. Harris, "Method for Measuring Material Thickness Profiles," U.S. Patent #6,038,027, 2000.
10. M. Marcus, "Fiber Optic Interferometry for Industrial Process Monitoring and Control Application," *Proc. SPIE*, Vol. 4578, pp. 136-144, 2002.
11. J. Bush, P. Davis, and M. Marcus, "All Fiber Optic Coherence Domain Interferometric Techniques," *Proc. SPIE*, Vol. 4204, pp. 71-80, 2001.
12. G. J. Tearney *et al.*, "Rapid Acquisition of in vivo biological images by use of optical coherence tomography," *Opt. Lett.*, Vol. 21, No. 17, pp. 1408-1410, 1996.
13. M. V. Klein and T. E. Furtak, Optics (John Wiley & Sons, 1986), pp. 523-524.
14. Guide to the Expression of Uncertainty in Measurement, International Organization for Standardization, Geneva, 1995.
15. K. P. Birch and M. J. Downs, "Correction to the Updated Edlén Equation for the Refractive Index of Air," *Metrologia*, **31**, pp. 315-316, 1994.
16. T. Doiron and J. S. Beers, The Gage Block Handbook, *NIST Monograph 180*, 1995.
17. J. E. Decker and J. K. Pekelsky, "Uncertainty evaluation for the measurement of gauge blocks by optical interferometry," *Metrologia*, **34**, pp. 479-493, 1997.
18. Starrett Catalog No. 29s, pg. 540, 1998.
19. P. R. Bevington and D. K. Robinson, Data Reduction and Error Analysis for the Sciences (2d ed. McGraw Hill, 1992), pp. 96-114.
20. W. H. Press *et al.*, Numerical Recipes in C: The Art of Scientific Computing (Cambridge University Press, 1990), pp. 523-528.

Downloaded From: https://www.spiedigitallibrary.org/conference-proceedings-of-spie on 10 Apr 2020
Terms of Use: https://www.spiedigitallibrary.org/terms-of-use